Icarus 343 (2020) 113711

Contents lists available at ScienceDirect

Icarus

journal homepage: www.elsevier.com/locate/icarus

Tides in subsurface oceans with meridional varying thickness

Marc Rovira-Navarro [a,d,*], Theo Gerkema [a], Leo R.M. Maas [c,b], Wouter van der Wal [d], Ron van Ostayen [e], Bert Vermeersen [d,a]

[a] NIOZ Royal Netherlands Institute for Sea Research, Department of Estuarine and Delta Systems EDS, Utrecht University, P.O. Box 140, 4400 AC Yerseke, the Netherlands
[b] NIOZ Royal Netherlands Institute for Sea Research, Department of Ocean Systems OS, Utrecht University, P.O. Box 59, 1790 AB Den Burg, Texel, the Netherlands
[c] Department of Earth Sciences, Faculty of Geosciences, Utrecht University, P.O. Box 80.121, 3508 TA Utrecht, the Netherlands
[d] TU Delft, Faculty of Aerospace Engineering (AE), Building 62 Kluyverweg 1, P.O Box 5058, 2629 HS Delft/2600 GB Delft, the Netherlands
[e] TU Delft, Faculty of Mechanical, Maritime and Materials Engineering (3mE), Mekelweg 2, 2628 CD Delft, the Netherlands

ARTICLE INFO

Keywords:
Tides
Icy moons
Rotational dynamics

ABSTRACT

Tidal heating can play an important role in the formation and evolution of subsurface oceans of outer-planet moons. Up until now tidal heating has only been studied in subsurface oceans of spatially uniform thickness. We develop a numerical model to consider oceans of spatially variable thickness. We use the Laplace Tidal Equations for the ocean and model the ice shell using membrane theory. The problem is solved using the commercial Finite Element software Comsol Multiphysics®. We use this new model to study the tidal response of Enceladus' ocean with a twofold objective: to understand how ocean thickness variations modify the tidal response of a subsurface ocean and to assess if tidal dissipation in an Enceladan ocean with varying ocean thickness can explain the high heat flux emanating from Enceladus' South Polar Terrain and the perdurance of a subsurface ocean. We consider the effect of meridional ocean thickness changes of spherical harmonic degree two and three as suggested by topography and gravimetry data. We observe that an ocean with degree two topography responds with the same eigenmodes as an ocean of constant thickness but resonances occur for thicker oceans. However, resonant ocean thicknesses are still thin compared to current estimates for Enceladus ocean thickness. Rossby-Haurwitz waves, excited by the obliquity tide for thick oceans of constant thickness, are not excited at the tidal frequency when oceans of variable thickness are considered. This result implies that the role of the obliquity tide in ocean tidal-dissipation might have been overestimated for Enceladus and other icy worlds. An antisymmetric, degree-three ocean thickness variation mixes the ocean modes excited in a constant thickness ocean by the eccentricity and obliquity tide.

1. Introduction

The discovery of subsurface oceans in the outer solar system (e.g., Kivelson et al., 1996; Khurana et al., 1998; Iess et al., 2014; Beghin et al., 2010; Saur et al., 2015; Thomas et al., 2016; Beuthe et al., 2016) has raised new questions on the thermal evolution of icy moons. Because they receive little energy from the Sun, the persistence of subsurface oceans in these bodies needs to be explained by internal heat sources such as radiogenic heating and tidal dissipation and/or the presence of dissolved salts or ammonia that decrease water's melting temperature. Tidal dissipation arises due to the non-zero obliquity and eccentricity of synchronously rotating icy satellites. It has long been recognised that tidal dissipation in solid viscoelastic layers can generate enough heat to maintain subsurface water reservoirs (e.g., Cassen et al., 1979). This is the case of the Jovian satellites Europa, Ganymede and Callisto, where models including radiogenic and tidal heating predict the presence of subsurface oceans (e.g., Ojakangas and Stevenson, 1989; Hussmann et al., 2002; Spohn and Schubert, 2003). However, for Enceladus, tidal heating in the solid layers of the moon is not enough to explain the presence of a global ocean (Tobie et al., 2008; Běhounková et al., 2017; Souček et al., 2019) unless the satellite rocky core is unconsolidated (Choblet et al., 2017). Neither can it account for the 10–50 GW of average tidal dissipation suggested by astrometric observations (Lainey et al., 2012, 2017; Nimmo et al., 2018) and the 4.2 GW of heat

* Corresponding author at: NIOZ Royal Netherlands Institute for Sea Research, Department of Estuarine and Delta Systems EDS, Utrecht University, P.O. Box 140, 4400 AC Yerseke, the Netherlands.
E-mail address: marc.rovira@nioz.nl (M. Rovira-Navarro).

https://doi.org/10.1016/j.icarus.2020.113711
Received 9 October 2019; Received in revised form 22 January 2020; Accepted 19 February 2020
Available online 27 February 2020

emanating from Enceladus' South Polar Terrain (SPT) observed by Cassini's CIRS instrument (Spencer et al., 2013). This fact has led to the speculation that oceanic tidal dissipation contributed significantly to the thermal budget of subsurface oceans (e.g., Tyler, 2008).

In the last decade, the role of ocean dynamics in tidal-dissipation has been investigated. Tyler (2008, 2009, 2011, 2014) considered the response of an ice-free ocean to tides, Matsuyama (2014) expanded the formulation to consider the effect of self-gravity and a deformable rocky core. More recently, models that consider the overlying ice shell have been developed (Beuthe, 2016; Matsuyama et al., 2018; Hay and Matsuyama, 2017, 2019). The ocean response highly depends on the surface gravity wave speed (c) which is given by $\sqrt{gh}$, with g being the ocean surface gravity and h the ocean thickness. The time it takes for a perturbation to travel around the moon is $2\pi R/c$, with R the moons's radius. If this time is much smaller than the tidal period, the ocean responds following nearly the equilibrium tide and oceanic tidal dissipation becomes negligible. Otherwise, the dynamic response of the ocean needs to be considered. Resonant ocean thicknesses exist for which tidal dissipation becomes very high. However, these resonances happen for oceans considerably thinner than those present on the moons of the outer solar system (e.g., Tyler, 2014; Matsuyama et al., 2018). It has been suggested that these resonances can prevent subsurface oceans from freezing as they get thinner (Tyler, 2011), although this may not be the case for small satellites like Enceladus where the effective rigidity of the ice shell is large (e.g., Hay and Matsuyama, 2019).

The obliquity tide can also excite (planetary) Rossby-Haurwitz waves (Tyler, 2008). Contrary to surface gravity waves, the restoring force lies in the conservation of potential vorticity (the fluid dynamical analog of angular momentum conservation) arising in a field where background vorticity varies spatially (such as due to a latitudinal gradient in planetary vorticity, or due to thickness-variations of a rotating fluid). These waves are characterised by an ocean flow that is tangentially non-divergent implying that there are no surface displacements in the radial direction. Rossby-Haurwitz waves were argued to play a major role in preventing Enceladus and Europa's ocean from freezing (Tyler, 2008, 2009, 2011). However, this argument relied on what is likely a two orders of magnitude overestimate of the obliquity of Enceladus (Chen and Nimmo, 2011) and the debate on the role of tidal heating in the ocean of Enceladus was reopened.

All of the previous studies are restricted to oceans of constant thickness. However, it is expected that subsurface oceans have thickness variations. For instance, gravity and topography data suggests that Enceladus' ocean thickness is not constant: the ice shell has degree two and three meridional thickness variations (Beuthe et al., 2016; Čadek et al., 2016; Hemingway and Mittal, 2019). On Earth, tides are greatly affected by ocean bathymetry, which raises the question of how the tidal response of a subsurface ocean of variable thickness differs from that of an ocean of constant thickness. In particular, we want to understand what the effect of ocean thickness variations is on gravity waves resonances and the excitation of Rossby-Haurwitz waves.

To tackle these questions we use a finite element software package Comsol Multiphysics® to solve the Laplace Tidal Equations for an ocean with varying thickness. To account for the ice shell we use the thin shell theory of Beuthe (2008, 2016) in the membrane limit. We consider a subsurface ocean overlying a rigid spherical core and neglect the effects of self-gravity. While our method can illustrate the effect of ocean thickness changes for subsurface oceans in general, we focus on Enceladus as there is compelling evidence for meridional ocean thickness variations and closing its thermal budget has proven to be more problematic than for other icy worlds (Nimmo et al., 2018). We start by considering an ocean of constant thickness and its solutions and then add meridional degree two and three ocean thickness variations via the dependence of phase speed on ocean thickness, while formally keeping the thickness of the elastic lid constant. This implicitly corresponds to an ocean with bedrock topography (Fig. 1). Even though our model has limitations (no self-gravity, a rigid core and constant ice shell thickness), it provides the first insight on how ocean thickness variations change the dynamic tidal response of subsurface oceans.

2. Problem formulation and assumptions

The Laplace Tidal Equations (LTE) were presented by Laplace (1798) in his study of barotropic (surface) tides. We use the formulation given in Tyler (2011). The linearised LTE for an ocean of variable thickness h and surface gravity g on a spherical body with radius R rotating at angular frequency Ω are given by:

$$\partial_t \boldsymbol{s} - f\boldsymbol{s}\times\boldsymbol{r} = -c^2\nabla\left(m - m_f\right) - F_{diss}, \tag{1a}$$

$$\partial_t m + \nabla\cdot\boldsymbol{s} = 0, \tag{1b}$$

where c is the local surface gravity wave phase speed that is a function of ocean thickness, f the Coriolis parameter ($2\Omega\cos\theta$ with θ being co-latitude), m_f a potential forcing term and $\boldsymbol{r}$ the unit radial vector. m and $\boldsymbol{s}$ are respectively a surface density and a vertically integrated momentum flow defined as:

$$m = \rho_w \eta, \tag{2}$$

$$\boldsymbol{s} = \int_h \rho_w \boldsymbol{u} dr. \tag{3}$$

ρ_w is the ocean density (assumed to be constant), and η and $\boldsymbol{u}$ are the radial surface displacement and tangential flow velocity. The forcing term m_f follows from the tidal potential Γ:

$$m_f = \frac{\rho_w}{g}\Gamma. \tag{4}$$

The term F_{diss} is a dissipative term that can take different forms. It is often described using a linear drag term, a quadratic drag terms or a combination of both:

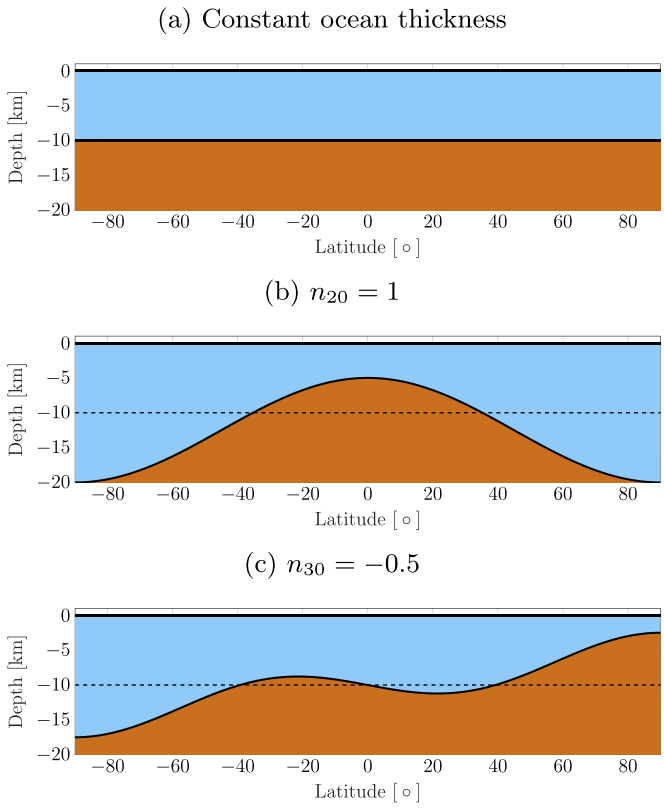

Fig. 1. Ocean thickness for a uniform ocean 10 km thick (a) and oceans with degree two (b) and three (c) meridional thickness variations.

$$F_{diss} = \alpha \boldsymbol{s} + \left(\frac{c_D g^2}{c^4 \rho_w}\right)\boldsymbol{s}|\boldsymbol{s}|. \quad (5)$$

α and c_D are the Rayleigh and the bottom drag coefficient, respectively. Differences between both approaches are discussed in detail in Hay and Matsuyama (2017). For a given bottom drag coefficient, scaling relations can be used to estimate a linear drag coefficient (Matsuyama et al., 2018). As most studies have considered the simpler case of linear drag (e.g., Tyler, 2011; Matsuyama, 2014; Matsuyama et al., 2018) and we want to investigate how the response of an ocean with variable thickness compares with an ocean of constant thickness we adopt the simpler linear approach.

If a pressure load q (positive inwards) acts on the ocean surface (e.g., atmospheric pressure, force exerted by an elastic lid), Eq. (2a) can be modified as:

$$\partial_t \boldsymbol{s} - f\boldsymbol{s}\times\boldsymbol{r} = -c^2\nabla(m - m_f + q/g) - \alpha\boldsymbol{s} \quad (6a)$$

$$\partial_t m + \nabla\cdot\boldsymbol{s} = 0. \quad (6b)$$

A problem that can arise depending on the choice of coordinates is the "pole-problem": nodes located at the poles become singular as the definition of east-west becomes singular (Platzman, 1978; Hay and Matsuyama, 2017). To avoid this problem the equations can be rewritten using a Helmholtz decomposition. The momentum flow is split into curl-free (Φ) and divergence-free (Ψ) components:

$$\boldsymbol{s} = \nabla\Phi + \nabla\times(\Psi r) \quad (7)$$

By using this definition and taking the curl and divergence of Eq. (6a), Eqs. (6a), (6b) become (Tyler, 2011):

$$\partial_t m + \nabla^2\Phi = 0, \quad (8a)$$

$$(\partial_t + \alpha)\nabla^2\Phi + f\nabla^2\Psi - \nabla f\cdot[(\nabla\Phi + \nabla\times(\Psi\boldsymbol{r})\times\boldsymbol{r}] = -c^2\nabla^2(m - m_f + q/g) - \nabla c^2\cdot\nabla(m - m_f + q/g), \quad (8b)$$

$$(\partial_t + \alpha)\nabla^2\Psi - f\nabla^2\Phi + \boldsymbol{r}\cdot[\nabla f\times(\nabla\Phi + \nabla\times(\Psi\boldsymbol{r}))\times\boldsymbol{r}] = \boldsymbol{r}\cdot[\nabla c^2\times\nabla(m - m_f + q/g)] \quad (8c)$$

From Eqs. (8b) and (8c) it becomes clear that ocean thickness variations enter the equations through the implicit dependence of c^2 on ocean thickness. In case of uniform c^2, we recover the equations for an ocean of constant thickness.

The term q couples the ocean and the ice shell response. Two different approaches have been used to account for this term: the thick and the thin shell approaches. The thick shell approach considers all the elements of the stress and strain tensor (Matsuyama et al., 2018). The thin shell theory is a 2D analog of the 1D beam theory. It can be used if the shell is thin compared with the radius of the body (i.e., 5–10% of the radius) (Beuthe, 2008). Under this circumstance it can be assumed that the transverse stress is negligible and that normals to the reference surface remain normal after deformation. The membrane limit is a further simplification that consists in neglecting bending within the ice shell. Matsuyama et al. (2018) and Hay and Matsuyama (2019) used the thick shell approach to study tidal dissipation in subsurface oceans, and showed that the membrane approach is accurate to 4% for Enceladus.

We use the thin shell approximation in the membrane limit. Beuthe (2008) derived a set of equations to study the deformation of a membrane of changing thickness under transverse and tangential loads. However these equations proved to be difficult to be efficiently implemented using Comsol's Multiphysics tools. The equations are fourth order differential equations which imply that quintic or higher order elements need to be used together with a high spatial resolution. This fact highly increases the computational time making it difficult to explore the parameter space. Due to this limitation we consider an ice shell of constant thickness which implies that changes in ocean thickness are implicitly represented by bedrock topography. In this case, the relation between surface displacements (η) and pressure exerted by the ice shell (q) is given by a second order differential equation:

$$\frac{1}{R}\Delta'\eta - \beta R\Delta' q + (1+\nu)\beta R q = 0. \quad (9)$$

ν is the Poisson ratio and β is extensional rigidity of an ice shell of constant thickness h_i and Young modulus E and is given by Beuthe (2008, 2016):

$$\beta = \frac{1}{E h_i}. \quad (10)$$

Δ' is a differential operator equal to $R^2\nabla^2 + 2$.

Eqs. (8a–c) and (9) can be solved to obtain the ocean response to tidal forcing. Once the ocean tidal response is obtained, the momentum flow s can be used to compute the amount of tidal dissipation for each time-step:

$$D = \int_S \frac{\alpha}{\rho_w h}\boldsymbol{s}\cdot\boldsymbol{s}dS. \quad (11)$$

D changes over a tidal-period. We are interested in the average tidal dissipation over a tidal-period, which is obtained as:

$$\overline{D} = \frac{1}{T}\int_T D dt \quad (12)$$

where T is the tidal period.

Eqs. (8a) and (8b) are forced through the tidal potential Γ which arises due to the eccentricity (e) and obliquity (ε) of the satellite. The tidal potential can be written in terms of the satellite's orbital elements (Jara-Orué and Vermeersen, 2011):

$$\Gamma = \omega^2 R^2(\psi_0 + \psi_{e0} + \psi_{e2e} + \psi_{e2w} + \psi_{o1e} + \psi_{o1w}), \quad (13)$$

where ω is the mean motion of the satellite which equals its rotational frequency Ω. ψ_0 is the static component of the tidal-potential which does not have any dynamic effect. The eccentricity and obliquity tide can be written in terms of spherical harmonics of degree two and different harmonic orders. The eccentricity tide consists of an order zero component (ψ_{e0}) and an order two component that can be further split into an eastward (ψ_{e2e}) and a westward component (ψ_{e2w}). The obliquity tide is an order one forcing that can also be split into eastward and westward components (ψ_{o1e}, ψ_{o1w}). These components are given by:

$$\psi_{e0} = -\frac{3e}{2}P_{2,0}\left(cos\theta\right)cos\left(\omega t\right), \quad (14a)$$

$$\psi_{e2e} = \frac{7e}{8}P_{2,2}(cos\theta)cos(2\phi - \omega t), \quad (14b)$$

$$\psi_{e2w} = -\frac{e}{8}P_{2,2}(cos\theta)cos(2\phi + \omega t), \quad (14c)$$

$$\psi_{o1e} = \frac{sin(\varepsilon)}{2}P_{2,1}(cos\theta)sin(\phi - \omega t + \Theta) \quad (14d)$$

$$\psi_{o1w} = \frac{sin(\varepsilon)}{2}P_{2,1}(cos\theta)sin(\phi + \omega t + \Theta) \quad (14e)$$

where e, ε and Θ are the satellite's eccentricity, obliquity and argument of pericenter, ϕ is fthe longitude and $P_{l,\,m}$ are associated Legendre polynomials of degree l and order m. The physical parameters used for Enceladus are given in Table 1.

3. Solving the LTE using FEM

Different approaches exist to solve the previous set of partial differential equations. If the ocean thickness is constant, spectral methods are very efficient (Longuet-Higgins, 1968; Tyler, 2011, 2014; Matsuyama, 2014; Matsuyama et al., 2018; Beuthe, 2016). In such methods, m, Φ, Ψ are expanded in a series of spherical harmonics and Eqs. (8a) and (8b) are reduced to a set of algebraic equations that can be inverted to obtain the spherical harmonic coefficients. However, if c^2 is not constant this approach is more problematic and other numerical

Table 1
Enceladus physical parameters used for this study. Physical and orbital parameters are obtained from the JPL ephemerides (http://ssd.jpl.nasa.gov/?sat_elem). Enceladus' obliquity is an upper bound obtained considering Enceladus is in a Cassini state (Baland et al., 2016). We use the same Young modulus (E), Poisson ratio (ν) and ocean density (ρ_w) as in Souček et al. (2016). Ocean (h_{ocean}) and ice shell thickness (h_{ice}) are varied within the indicated range.

Parameter	Value
R [km]	252.1
g [m s^{-2}]	0.11
Ω [rad s^{-1}]	$5.31 \cdot 10^{-5}$
e [−]	0.047
ε [°]	0.00045
Θ [rad]	0
ρ_w [kg m^{-3}]	1007
E [10^9 Pa]	8.778
ν [km]	0.33
h_{ocean} [km]	$0.01 - 45$
h_{ice} [km]	0,1,10
α [s^{-1}]	$1 \cdot 10^{-5,\ -6,\ -7}$

approaches are more suitable.

For example, for Earth, Platzman (1975) used a finite difference method to study the eigenmodes of the Atlantic ocean. The finite difference method presents some challenges, one of them being the previously mentioned "pole-problem". Platzman (1978) developed an alternative approach using a Finite Element Method (FEM) and applied it to study the eigenfrequencies and modes of Earth's ocean basins. In the context of planetary sciences, Sears (1995) used a finite difference approach to solve for tides in Titan's hydrocarbon lakes. This approach was incorporated in the first version of ODIS (Ocean Dissipation in Icy Satellites) (Hay and Matsuyama, 2017) to study tides in icy satellites with non-linear bottom drag. A finite volume method is used in the most recent version of ODIS (Hay and Matsuyama, 2019).

We use the commercial Finite Element software Comsol Multiphysics® to solve the system of partial differential equations. Comsol Multiphysics® allows to solve user-defined partial differential equations and has extensively tested build-in integration methods that can be employed (Comsol Multiphysics®, 2012). More specifically, we use the Boundary PDE module to solve the PDEs in the boundary of a 3D domain, in our case a sphere of radius R. The equations are discretised using a mesh of quadratic triangular elements. The use of quadratic elements gives a smooth representation of the derivatives of m, Φ, Ψ and therefore of the flow momentum s (see Eq. (7)) which results in a more accurate estimation of tidal dissipation for a given mesh size.

The eigenmodes and eigenfrequencies of the system are obtained using the eigenvalue solver algorithm of Comsol® which uses the implicitly restarted Arnoldi method (IRAM). Different methods can be used to integrate the system forward in time. Hay and Matsuyama (2017, 2019); Sears (1995) use an explicit method. This implies that the time step should fulfill the Courant-Friedrichs-Lewy (CFL) stability conditions which dictates that $\Delta t \leq \Delta l/c$ with Δl being the mesh size which places a stringent constraint on time-step for thick oceans. In contrast, we decide to use the Generalized-Alpha method, an implicit second-order integration method (Chung and Hulbert, 1993). The use of an implicit method has the advantage that the CFL condition can be relaxed.

The system is forced with the eccentricity and obliquity tide and integrated forward in time until a periodic solution is reached. The accuracy of the solution depends on the mesh-size and time step. Appendix A shows a benchmark of the FEM model as well as a study of the effect of mesh-size and time step. Based on the results presented there we decide to use a mesh with 834 elements (Fig. A.7) and a time step of 0.008 Enceladus orbital period for the simulations presented below. Using these parameters the error is shown to be smaller than 3% in most of the parameter space with the exception of few cases close to resonant states for which the error can be up to 20%.

4. Results

We use the FEM presented above to compute the response of subsurface oceans to the time-varying eccentricity and obliquity tidal potential (Eqs. 14a–e). We consider ocean thicknesses between 10 m and 45 km. For each ocean thickness we force the system with the eccentricity and obliquity tide, the solution approaches the periodic steady solution asymptotically. In order to speed-up convergence we follow the approach of Hay and Matsuyama (2017). Instead of using initial conditions of the rest state, we use the converged solution of the previous ocean thickness as starting point. For some ocean thicknesses, the ocean response exhibits oscillations with a period of few Enceladan orbits diminishing in amplitude (see Fig. A.8). For these cases we compute tidal dissipation by averaging tidal dissipation for the last oscillation.

The Rayleigh coefficient depends on the dissipation mechanism at work in the ocean. Using values of Earth's Rayleigh and bottom drag coefficients, Matsuyama et al. (2018) argues that its value can range from 10^{-5} s^{-1} to 10^{-11} s^{-1}. We consider a nominal Rayleigh coefficient of 10^{-7} s^{-1} and briefly discuss the effect of changing this parameter by exploring two more dissipative scenarios ($10^{-5,\ -6}$ s^{-1}).

We are interested in studying the effect of ocean thickness variations on the ocean response. However, to put our results into context, we start by considering the very thoroughly studied case of a global ocean of constant thickness without any ice-cover, then discuss the effects of adding an elastic ice shell of constant thickness and, finally, we study how ocean thickness variations alter the ocean response.

4.1. Ocean of uniform thickness

The case of a global ocean with a free surface (no ice shell) has been widely studied in the past in the context of geosciences (e.g., Hough, 1898; Longuet-Higgins, 1968) and recently revisited in the context of planetary sciences (e.g., Tyler, 2008; Matsuyama, 2014; Beuthe, 2016; Hay and Matsuyama, 2017). The behaviour of the system can be understood in terms of its eigenmodes and eigenfrequencies. Resonances can occur when the system is forced at one of its eigenfrequencies with a forcing that has a spatial pattern similar to that of the eigenmode. We will first consider the eigenmodes of Eqs. (8a), (8b), (9) without a forcing term and then the response of an ocean forced with the tidal potential. For the discussion that follows, we will name the different modes as follows: the first letter indicates whether the mode is symmetric (S) or antisymmetric (A) with respect to the equator; the number that follows indicates the order of the mode (wave number in the longitudinal direction), and the second letter indicates the propagation direction: east (E), west (W) or standing non-propagating wave (-). As some modes share the previous characteristics we will use subindices to distinguish modes belonging to the same family, with 1 corresponding to the mode excited for the thickest ocean.

It is very common to study the LTE in terms of the non-dimensional Lamb parameter $\varepsilon = 4\Omega^2 R^2/gh$ (e.g., Hough, 1898; Longuet-Higgins, 1968). In his pioneering work, Hough (1898) studied the response of a non-dissipative ocean in the limit of a thick ocean $h \to \infty$ (or $\varepsilon \to 0$) and identified two classes of waves: waves of the first class (gravity-waves), and waves of the second class (vorticity waves).[1] He showed that the

[1] Vorticity waves were first discovered by Laplace (Laplace, 1798). These oscillations were forgotten until Margules (1893) and Hough (1898) rediscovered them independently and called them oscillations of second class. Rossby and Haurwitz (Rossby, 1939; Haurwitz, 1940) rediscovered the waves of the second class again and since then the term "Rossby-Haurwitz waves" or "planetary waves" is also widely used to refer to Class 2 oscillations. We use both terms depending on the context.

eigenfrequencies (in the asymptotic limit) are respectively given by:

$$\frac{\omega}{2\Omega} = \sqrt{\frac{n(n+1)}{\varepsilon}} \tag{15a}$$

$$\frac{\omega}{2\Omega} = \frac{m}{n(n+1)} \tag{15b}$$

where n and m are the degree and order of the ocean response. Class 2 oscillations propagate westward, while class 1 oscillations can propagate either east- or west- ward. Fig. 2 shows a representative Class 1 $(S2E)_1$ and Class 2 $(A1W)_1$ mode. The plots show the amplitude and phase of surface displacements (η) as well as the tangential flow velocity ($\boldsymbol{u}$) at t=0 (in red) and tidal ellipses showing the change of magnitude

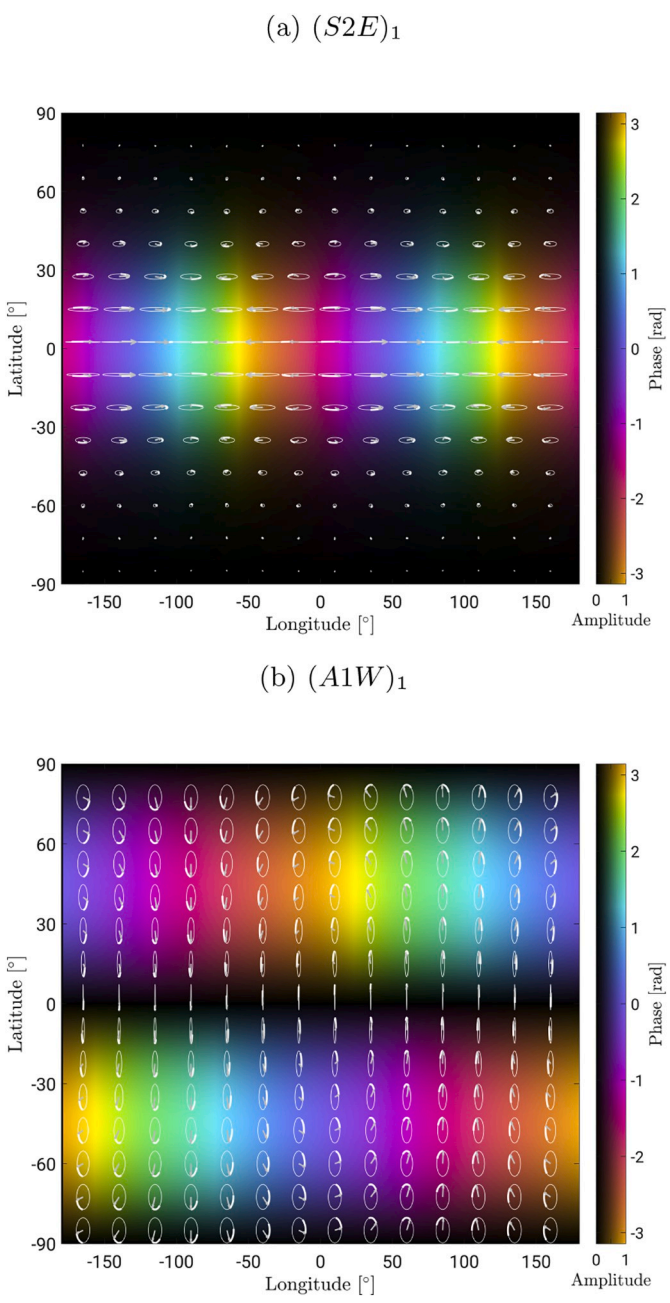

Fig. 2. Class 1 (a) and Class 2 mode (b). The arrows show the flow velocity at t=0, the surrounding ellipses show the change of the flow velocity during a tidal period. The phase and amplitude of surface displacements are shown in the background, with the phase represented by the colour and amplitude by brightness. Black indicates diminishing amplitude.

and direction of the current vector over a tidal period. The difference between these two modes can be further appreciated by computing the ratio of potential energy to total energy (kinetic plus potential). For an ocean thickness of 10 km this ratio equals 0.4659 for the Class 1 $(S2E)_1$ mode and 0.016 for the Class 2 $(A1W)_1$ mode, indicating that surface displacements are small for the $(A1W)_1$ mode which means that the flow is nearly non-divergent. As ocean thickness increases, the ratio approaches 0.5 and 0 for Class 1 and 2 modes, respectively (Longuet-Higgins, 1968, Figures 14, 15).

The eigenfrequencies of the system for different ocean thicknesses are shown in Fig. 3. The modes that have the right spatial structure to be excited by the eccentricity and obliquity tide are labelled. For an ocean of constant thickness symmetric and antisymmetric modes with respect to the equator are decoupled. Therefore the symmetric eccentricity tide excites symmetric modes while the antisymmetric obliquity tide excites antisymmetric modes. These modes are shown in Figs. B.9 and B.10, where the distinction between symmetric and antisymmetric modes can be identified as a 180° phase lag between the Northern and Southern Hemisphere. The order of the mode is evident as the number of cycles in the zonal direction. Class 2 modes can be distinguished in Fig. 3 as modes which asymptotically approach a constant frequency. This is the case of the $(A1W)_1$ mode which in the asymptotic limit has an eigenfrequency equal to that of the tidal forcing $\omega/2\Omega$=0.5. By contrast, the other indicated modes are Class 1 modes whose frequency in the thick ocean limit is proportional to $h^{1/2}$ and therefore show up as straight lines of slope 1/2 in Fig. 3.

As the ocean becomes thinner the spectrum becomes denser and we cannot use the classification into Class 1 and 2 modes anymore. In the limit $h \to 0$ ($\varepsilon \to \infty$), Longuet-Higgins (1968) distinguished three types of modes. For the first type, the eigenfrequency is proportional to $h^{1/4}$ while for the second and third type it is proportional to $h^{1/2}$. The second and third type can be distinguished because they propagate westward and eastward respectively. All modes labelled in Fig. 3 are type 1 except mode $(S2E)_1$ which is type 3 as evidenced by its slope. In between the two asymptotic limits ($\varepsilon \to \infty$ and $\varepsilon \to 0$) the eigenfrequency curves change their slope as they transition to class 1 and 2 oscillations.

When forced with the tidal potential, the response of the system is given by a combination of the previous eigenmodes. The tidal response is maximized if the eigenfrequency of the mode is the same as the tidal frequency, which can be visualised as a mode crossing the horizontal line corresponding to $\omega/2\Omega$=1/2 in Fig. 3. When this happens a resonance occurs. Fig. 4 shows the average tidal dissipation for different ocean thicknesses due to the eccentricity and obliquity tide. The ocean response is characterised by a series of resonance peaks, i.e. ocean thicknesses for which tidal dissipation is enhanced by several orders of magnitude. For these resonant peaks, tidal dissipation can be above Enceladus' observed thermal flux (Spencer et al., 2013). The resonance peak corresponding to a thicker ocean occurs for an ocean thickness of h_o=363 m. However, as noted before, the actual ocean on Enceladus is expected to be much thicker (Beuthe et al., 2016). Surface heat flux patterns due to the eccentricity tide for a resonant and non-resonant configuration are shown in Fig. 5a, b. In both cases tidal dissipation is symmetric and maximum in equatorial regions, for the resonant ocean thickness tidal dissipation is increased by 7 orders of magnitude. Dissipation patterns depend on flow amplitudes, from the eigenmodes depicted in Fig. B.9, it follows that tidal dissipation in polar regions is very small for the eccentricity tide which does not agree with Cassini's observation of enhanced heat flux in Enceladus SPT.

The curves corresponding to the eccentricity and the obliquity tides are markedly different. Dissipation due to Enceladus' obliquity is lower than that due to its eccentricity, mainly because the obliquity of Enceladus is predicted to be very small (see Table 1). Moreover, the behaviour for an increasing ocean thickness differs. For the eccentricity tide we observe that tidal dissipation decreases with ocean thickness. As the ocean thickness increases the surface gravity wave-speed increases too, thus the ocean can adjust faster to the varying tidal potential.

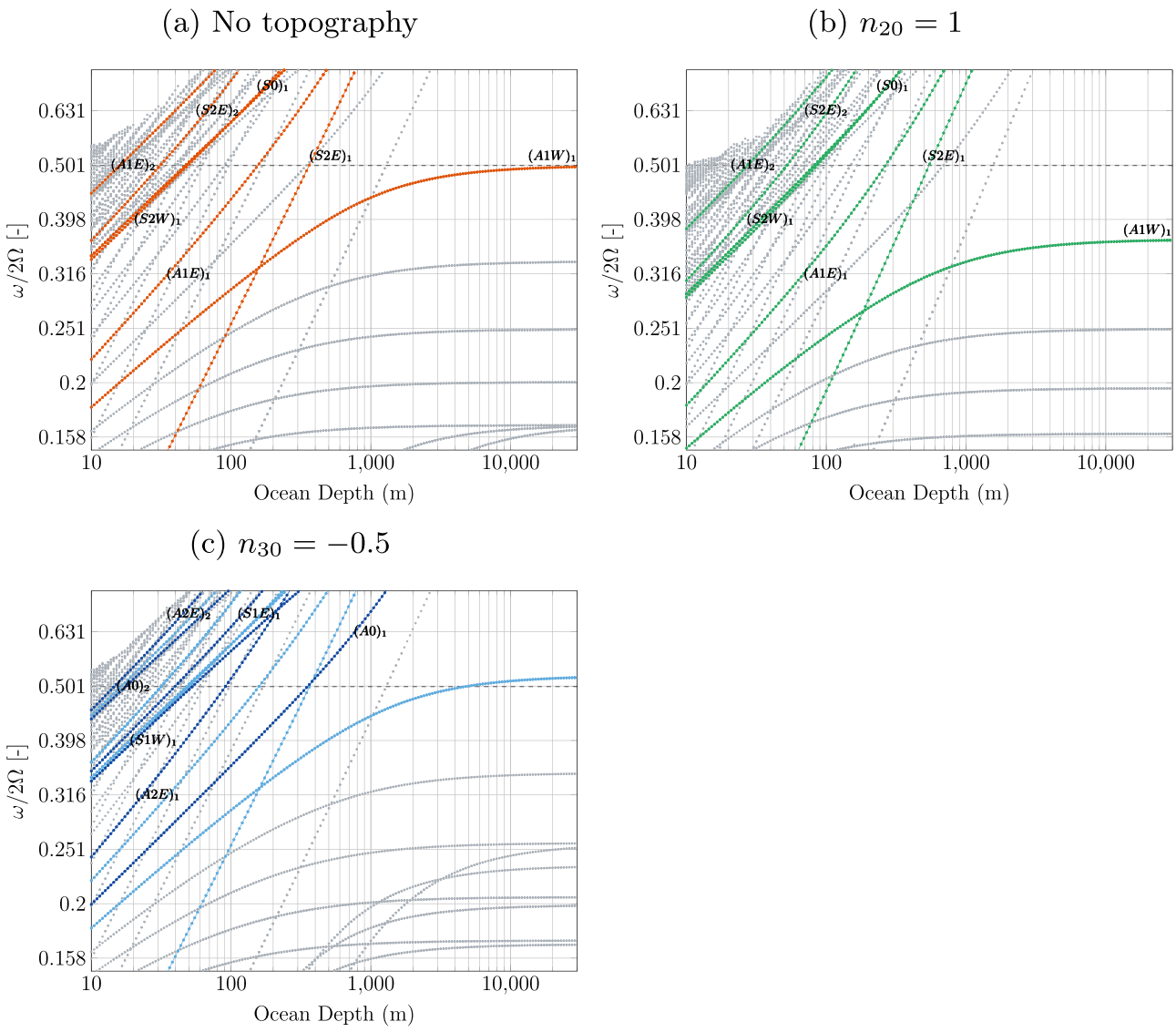

Fig. 3. Eigenfrequencies for an ocean without ice cover and different ocean thickness changes. The modes excited by the obliquity tide and the eccentricity tide are indicated. For the ocean with degree three order zero topography only the new excited modes (indicated in darker blue) are labelled. High frequency eigenmodes corresponding to thin oceans (upper left corner) are not shown. (For interpretation of the references to colour in this figure legend, the reader is referred to the web version of this article.)

Interestingly, this is not the case for the obliquity tide, which shows the opposite behaviour. This is because the ocean response is mainly given by the Rossby-Haurwitz mode $(A1W)_1$. We should not label this behaviour as a resonance (Beuthe, 2016). In contrast to the other resonance peaks, where in the inviscid limit kinetic energy diverges as the difference between eigenfrequency and forcing frequency becomes smaller, the excitation of the $(A1W)_1$ mode does not result in a divergent response. Dissipation patterns for this mode are shown in Fig. 5c. Contrary to the eccentricity tide, where tidal dissipation is maximum at the equator, tidal dissipation is enhanced at the poles for the obliquity tide. However, dissipation patterns remain symmetric and the values are still small compared with the estimated radiogenic heating ($\sim 4 \times 10^{-4}$ Wm^{-2}) making it difficult to explain Enceladus dichotomy through this mechanism.

The ocean response is influenced by the value of the Rayleigh coefficient. As expected, for more dissipative oceans (higher α) resonant peaks are smoothed (Fig. 4d, e). Similarly, lower values result in narrower resonance peaks but do not alter the ocean thickness for which they occur provided $\alpha \ll \Omega$. When damping is increased, the obliquity tide in the thick ocean limit is no longer only described by the Rossby-Haurwitz alone, gravity waves are added to the solution. In such cases, the maximum value of tidal dissipation is not obtained in the limit $h \to \infty$ (Matsuyama, 2014; Beuthe, 2016; Hay and Matsuyama, 2019).

If an ice shell is added the response of the system is altered. We compute the tidal response of an ocean of constant thickness covered by a 1 or 10 km ice shell. As in Beuthe (2016) and Matsuyama et al. (2018) we find that the effect of adding an elastic ice shell is twofold (Fig. 4): (1) it shifts the gravity mode resonance peaks to thinner oceans and (2) for thick oceans it dampens the ocean response. Using the $(S2E)_1$ mode as an example we can see that the ocean thickness for which this mode has an eigenfrequency equal to that of the tidal force decreases with increasing ice shell thickness (Fig. 6b), resulting in the shift of the resonance peaks. The $(A1W)_1$ mode still has an eigenfrequency equal to $\omega/2\Omega$=0.5 in the thick ocean limit and thus Rossby-Haurwitz waves are still excited by the obliquity tide in an ocean covered by an ice shell.

(a) $h_{ice} = 0$ km

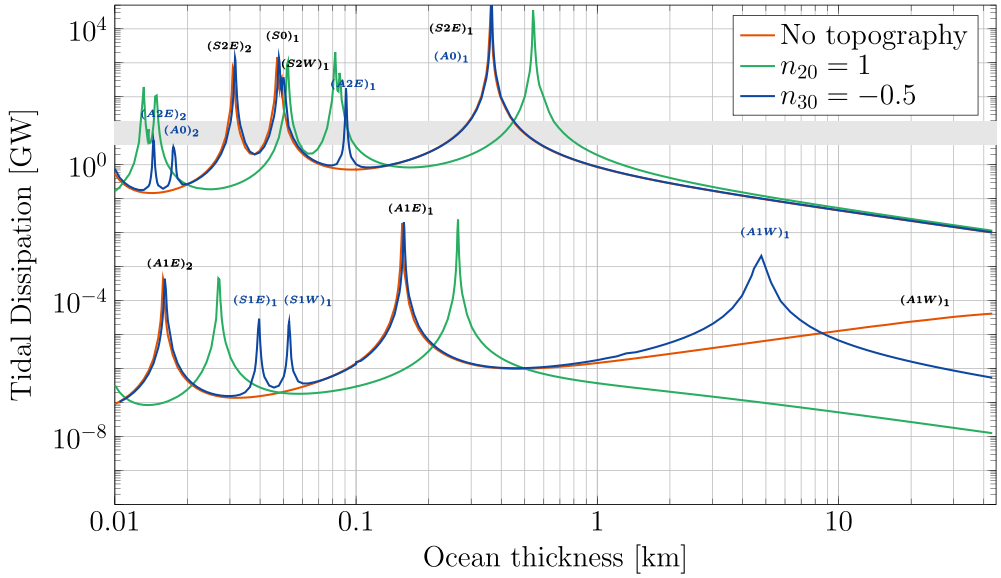

(b) $h_{ice} = 1$ km; $\alpha = 10^{-7}$ s^{-1}

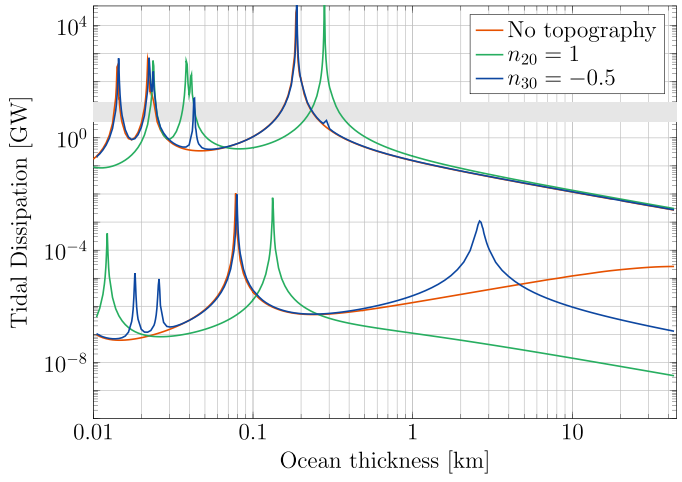

(c) $h_{ice} = 10$ km; $\alpha = 10^{-7}$ s^{-1}

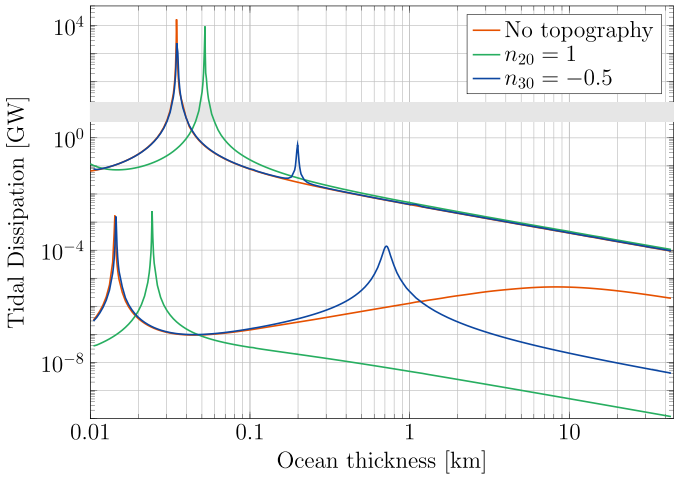

(d) $h_{ice} = 0$ km; $\alpha = 10^{-5}$ s^{-1}

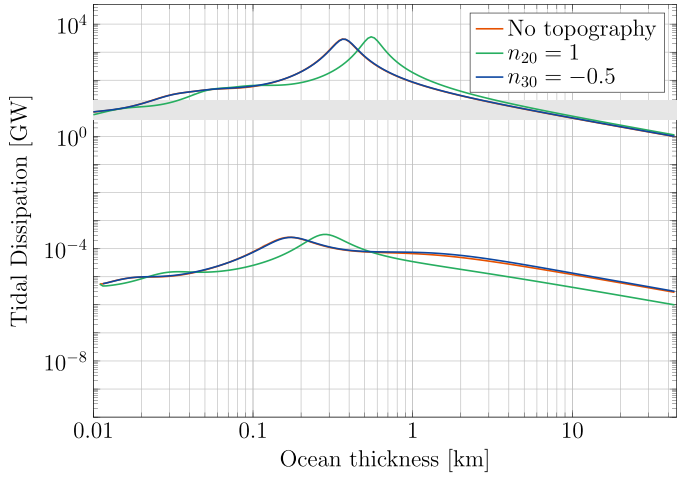

(e) $h_{ice} = 0$ km; $\alpha = 10^{-6}$ s^{-1}

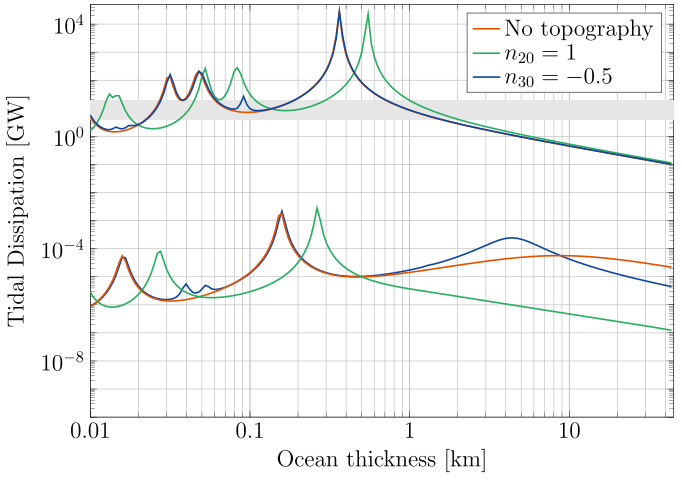

(caption on next page)

Fig. 4. Tidal dissipation for different ocean thicknesses for an ocean of constant thickness and oceans with degree two and three thickness topography. Each panel shows tidal dissipation due to the obliquity tide and eccentricity tide with the curves for the obliquity tide corresponding to lower values of tidal dissipation. The different panels show the solution for different ice shell thicknesses (0,1 and 10) km and Rayleigh coefficient (10^{-5}, 10^{-6}, 10^{-7}) s^{-1}. In (a) the different resonances are labelled, those excited due to antisymmetric topography are indicated in blue. The horizontal grey band corresponds to the observed thermal output of Enceladus (Spencer et al., 2013). (For interpretation of the references to colour in this figure legend, the reader is referred to the web version of this article.)

4.2. Ocean of variable thickness

Using gravity, topography and libration data Beuthe et al. (2016), Čadek et al. (2016) and Hemingway and Mittal (2019) showed that Enceladus' ice shell has degree two and three thickness changes resulting in ocean thickness variations of the same type. As explained in Section 2, our model uses an ice shell of constant thickness; ocean thickness variations are therefore implicitly given by sea-floor topography. We consider an ocean with thickness variations of the same kind as those inferred for Enceladus' ice shell:

$$h = \hat{h}(1 + n_{20}P_{20} + n_{30}P_{30}) \tag{16}$$

where $\hat{h}$ is the average ocean thickness and P_{20} and P_{30} are respectively the degree two and three order zero Legendre functions. These two types of ocean topography are shown in Fig. 1. Their effect will be studied separately.

The values of n_{20} and n_{30} depend on ocean and ice shell geometry. For a 38 km thick ocean and an ice shell of 22.8 km, Beuthe et al. (2016) obtains values for n_{20} and n_{30} equal to $\sim$0.3 and ~ -0.1, respectively. To make the effect of variable ocean thickness more evident we use higher nominal values of n_{20} and n_{30} equal to 1 and -0.5, respectively.

We start by considering how symmetric ocean thickness changes affects the ocean response. We compute tidal dissipation due to the eccentricity and the obliquity tide, the results are shown in Fig. 4. Some

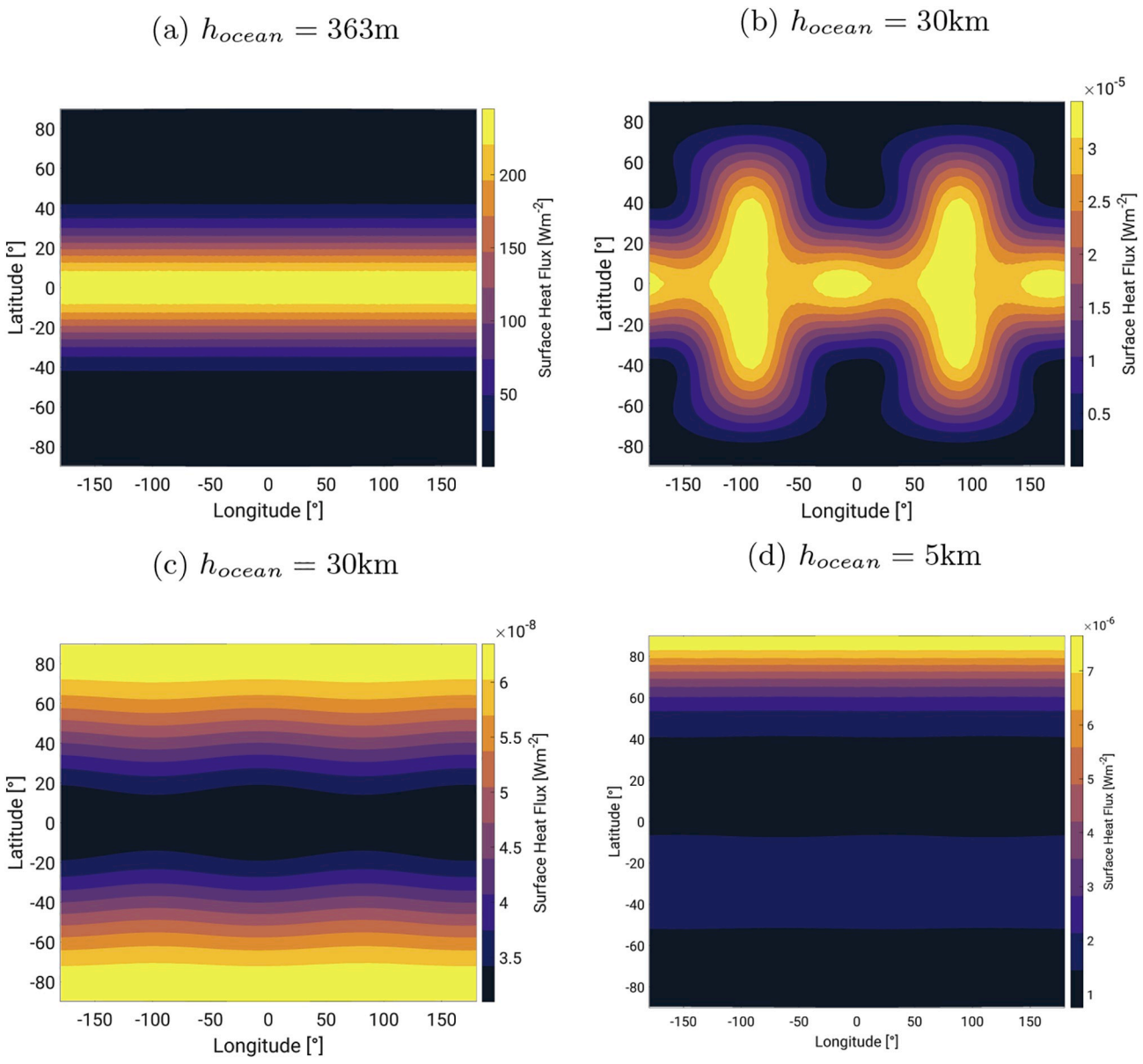

Fig. 5. Time-averaged tidal dissipation patterns for the eccentricity (a, b) and obliquity tide (c, d) in an ice-free ocean. (a, b, c) show dissipation patterns for an ocean of constant thickness while (d) correspond to an ocean with degree three topography.

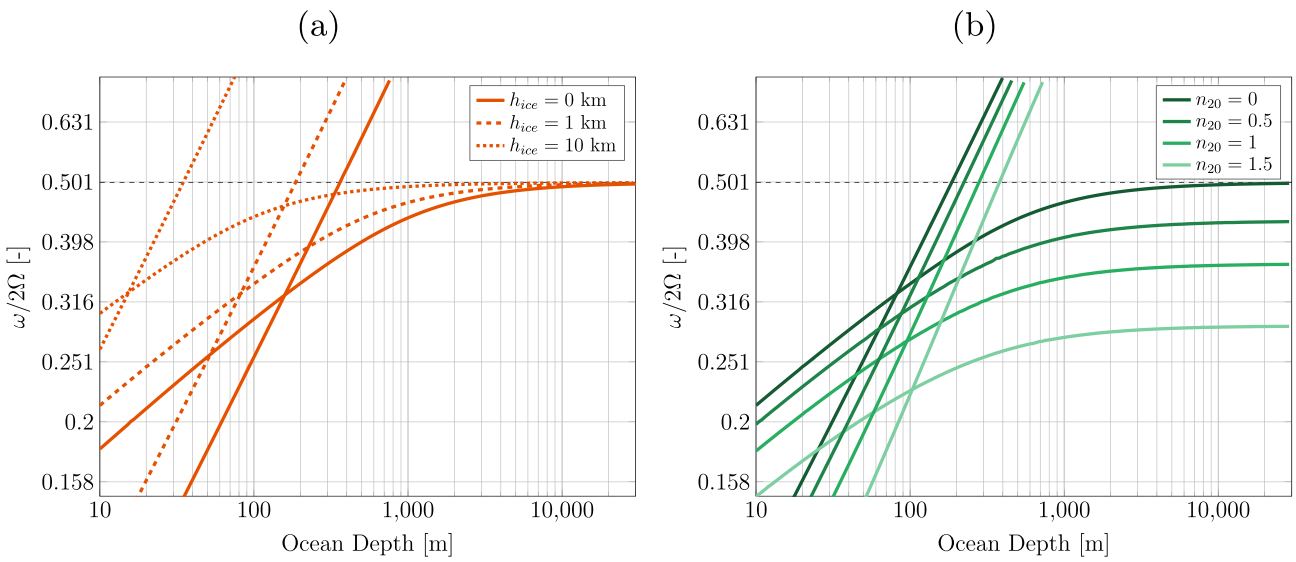

Fig. 6. Eigenfrequencies for the $(S2E)_1$ (straight lines) and $(A1W)_1$ (bended lines) modes for an ocean of constant thickness and different ice shell thicknesses (a), and an ocean with a 1 km ice shell and different amplitudes (n_{20}) of degree two topography.

differences are apparent when comparing the tidal response to that of an ocean without topography. Firstly, the same resonant peaks characteristic of an ocean of constant thickness are observed, however, they are shifted towards thicker oceans. For the case of an ocean with a free-surface the $(SE2)_1$ resonance moves from a 363 to a 550 m deep ocean. Secondly, we observe that, oppositely to what occurs when the ocean is uniform, tidal dissipation decreases with increasing ocean thickness for the obliquity tide which suggests that the Rossby-Haurwitz mode $(A1W)_1$ is not efficiently excited in an ocean with degree two topography.

Some further insight can be obtained by considering the eigenmodes of the system when topography is included. Fig. 3b, shows the eigenfrequencies of the system for n_{20}=1. We observe that the general appearance of the spectrum is not very different from that of a uniform ocean. The ocean thicknesses at which the gravity modes cross the tidal frequency line change, which translates in the shift of resonance peaks observed in Fig. 4. In contrast, the Rossby-Haurwitz $(A1W)_1$ mode approaches a frequency lower than the forcing frequency in the thick ocean limit, which diminishes the role of this mode. As we did before for different ice shell thicknesses, we track the $(A1W)_1$ and the $(S2E)_1$ modes for different values of n_{20} (Fig. 6b). The $(S2E)_1$ resonance gradually shifts towards thicker oceans as n_{20} increases and the asymptotic Rossby-Haurwitz eigenfrequency decreases.

We move now to the case of oceans with antisymmetric ocean thickness changes. The dissipation curve corresponding to an ocean with antisymmetric thickness variations is similar to that of an ocean of constant thickness (Fig. 4). However, we observe that new resonant peaks corresponding to new modes appear (labelled in blue in Fig. 4). We will first discuss the effect of degree three topography in the modes already present in the constant thickness ocean response and then examine the new modes.

With the exception of the $(A1W)_1$ mode, the modes also excited for a constant thickness ocean occur for roughly the same ocean thickness as in the constant ocean thickness case. This fact contrasts with degree two topography, where we observe a shift in the resonance peaks towards thicker ocean. The different behaviour can be understood by examining the geographical patterns of the gravity modes excited by the eccentricity and obliquity tide (Figs. B.9 and B.10). We observe that these modes are confined to low and mid latitude regions. Thus, it can be expected that the ocean thickness in this latitudinal range will control the tidal response. Looking at Fig. 1 it is evident that an ocean with degree two topography deviates from an ocean of constant thickness in low and mid latitudes. For $n_{20}>0$ the ocean is thinner than the average ocean thickness; this means that at low and mid latitudes an ocean thickness similar to that for which the gravity modes are excited for a constant thickness ocean will be attained for a higher $\hat{h}$, explaining the shift towards higher $\hat{h}$ in the resonant peaks. In contrast, ocean thickness variations at low and mid latitudes for degree three topography are small (Fig. 1). This results in the terms related with ocean thickness variations in Eqs. (8a), (8b) to be small and results in gravity mode resonances occurring approximately for the same average ocean thickness ($\hat{h}$) as in the constant thickness ocean.

In contrast, the $(A1W)_1$ mode (Fig. 2b) is not confined to low latitudes and thus the previous argument does not apply. The ocean response is more affected by degree three thickness variations which are large at high latitudes. As in the constant thickness ocean, we observe that the $(A1W)_1$ mode eigenfrequency asymptotically approaches a constant frequency in the limit $h \to \infty$ in Fig. 3c. However, this asymptotic frequency is higher than the tidal frequency. Therefore the mode crosses the tidal frequency line and as a consequence dissipation due to the $(A1W_1)$ mode reaches a maximum and then decreases with increasing ocean thickness. We obtain tidal dissipation patterns for this mode and compare them with the same mode for a uniform ocean (Fig. 5c, d). Degree three topography results in anti-symmetric tidal dissipation patterns, tidal dissipation is enhanced in north polar regions, where the ocean is shallow. This simply follows from mass conservation, Eq. (6b); currents are stronger in shallower regions which results in higher energy dissipation. Although this mechanism presents a new way to introduce anti-symmetries in tidal dissipation patterns it does not agree with Enceladus heat flux being higher at the Southern Hemisphere.

As mentioned before, new modes are excited when the antisymmetric topography is considered. The new modes are shown in Fig. B.11. As opposed to the two previous cases we notice that antisymmetric modes $(A2E)_{1,\,2}$ and $(A0)_{1,\,2}$ are excited by the symmetric eccentricity tidal forcing and the symmetric modes $(S1E)_1$ and $(S1W)_1$ are excited by the antisymmetric obliquity forcing. Fig. 3c shows the eigenfrequencies of the modes excited by the eccentricity and obliquity tide. Indicated in dark blue are the new modes that appear due to the degree three order zero topography. The $(A0)_1$ resonance is particularly interesting. For an ice-free ocean, its resonance thickness is the same as that of the $(S2E)_1$ mode and thus it is shadowed by this mode in the dissipation curve.

Adding an ice shell separates the two modes and the $(A0)_1$ mode becomes visible in the dissipation curves (Fig. 4b, c) to the right of the $(S2E)_1$ resonance peak for the 1 and 10 km thick ice shells.

5. Conclusions

In this paper we present a new numerical model to solve ocean tides in subsurface oceans with variable thickness. We solve the Laplace Tidal Equations for an ocean of variable thickness coupled with an elastic membrane of constant thickness. We use the Boundary PDE module of the commercial finite element software Comsol Multiphysics®. The equations are spatially discretised using quadratic triangular elements and integrated in time using the Generalized Alpha algorithm. We benchmark the model against the solution of the LTE for an ocean of constant thickness obtained by Matsuyama (2014) using a spectral method. We show that the model converges to the analytic solutions of Matsuyama (2014) provided that sufficiently small time steps and mesh size are used.

We use this model to study tides in Enceladus' subsurface ocean. We start with the thoroughly studied case of an ocean of constant thickness to identify characteristics in the system that help us understand the response for an ocean with variable thickness (e.g. Tyler, 2008; Beuthe, 2016; Hay and Matsuyama, 2019). As in previous studies, we find that the ocean response to the eccentricity and obliquity tide is characterised by a series of resonant peaks where tidal dissipation surpasses Enceladus's observed heat flux (Spencer et al., 2013) but does not agree with the observed distribution of heat. The resonant peaks can be related to the eigenmodes of the system. The equatorially symmetric eccentricity tide excites symmetric modes while the anti-symmetric obliquity tide excites anti-symmetric modes. All the excited modes are gravity-waves modes except for the westward propagating Rossby-Haurwitz mode which corresponds to a vorticity (or Class 2) mode. Gravity mode resonances occur for oceans that are thinner (few hundred meters) compared to the average ocean thickness of around 30 km estimated using gravity, libration and altimetry data (Beuthe et al., 2016; Čadek et al., 2016; Hemingway and Mittal, 2019). The Rossby-Haurwitz mode is excited by the obliquity tide for thick oceans which results in an increase of tidal heating with ocean thickness for the obliquity tide.

We then explore the effect of degree two and three meridional ocean thickness variations in the ocean response. We observe that the equatorially symmetric degree two topography does not add additional resonant modes to the ocean response. However, the resonant ocean thicknesses for the gravity wave modes are shifted to thicker oceans than those of an ocean of uniform thickness. This shift does not push the resonant ocean thickness to a value close to Enceladus' estimated ocean thickness. The antisymmetric degree three topography can activate new resonant modes. We observe that equatorially symmetric modes can be excited by the antisymmetric obliquity tide and antisymmetric modes are excited by the symmetric eccentricity tide.

Topography also affects the excitation of Rossby-Haurwitz waves. For degree two topography, Rossby-Haurwitz waves have a frequency lower than the tidal frequency which limits the excitation of these waves by the obliquity tide. With degree three topography the maximum dissipation due to the Rossby-Haurwitz mode occurs for thinner oceans than in the constant ocean thickness case. Additionally, degree three topography results in anti-symmetric dissipation patterns, but maxima are attained at the north polar regions and not the south polar regions as observed by Cassini. These results have important implications as the Rossby-Haurwitz mode has been suggested to play a major role in preventing subsurface oceans in Europa (Tyler, 2008), Enceladus (Tyler, 2009) or Triton (Chen et al., 2014; Nimmo and Spencer, 2015; Hay and Matsuyama, 2019) from freezing. We show that an uneven ocean diminishes the amount of tidal heating produced through the excitation of Rossby-Haurwitz waves. These results are similar to those of Tyler (2011), who already pointed out that the Rossby-Haurwitz wave amplitude is greatly reduced in the case of an Enceladan ocean confined to the South Pole.

This study illustrates the importance of topography in controlling the tidal response of subsurface oceans. However, very little information on ocean thickness variations is available for icy moons. In the case of Enceladus, gravity, libration and altimetry data suggest degree two and three variations in the ice shell thickness (Beuthe et al., 2016; Čadek et al., 2016; Hemingway and Mittal, 2019). For Europa these lateral variations could be smaller (Nimmo et al., 2007) and they are unknown for other ocean worlds. Very little is known about seafloor topography, however low gravity objects like Enceladus can potentially support large topographic relief. Future missions such as JUICE or Europa Clipper might help to estimate ocean thickness for some of these bodies leading to a better understanding of tides in subsurface oceans.

Our numerical model has some limitations that should be pointed out. Firstly, it does not include self-gravity and the ocean is assumed to be covering a rigid core. Matsuyama (2014) showed that including the effect of self-gravity and considering a deformable core results in a shift of gravity mode resonances to thicker oceans. Moreover, self-gravity slightly enhances tidal dissipation per unit time due to the obliquity tide for thick oceans (Hay and Matsuyama, 2019). However, these two elements do not add new modes to the ocean response. Similar effects are expected if self-gravity and a deformable core would be added to our model. Secondly, while our ocean model includes meridional thickness variations through a thickness dependent phase speed we model the ice shell as an elastic membrane of constant thickness. This implies that ocean thickness variations are due to seafloor topography instead of ice shell thickness variations. Běhounková et al. (2017) and Souček et al. (2019) considered the response of Enceladus' ice shell of variable thickness above an ocean that is in hydrostatic equilibrium. Their ice shell model is 20 km thick on average and varies from about 5 km in the SPT to more than 30 km near the equator, additionally the Tiger Stripes are included as weak regions in the SPT. They showed that, when forced with the eccentricity tide, ice thickness variations lead to a higher amplitude of surface displacements in the SPT compared with a uniformly thick ice shell. Based on our results, we expect that this would result in the excitation of the antisymmetric ocean modes as happens with the degree three seafloor topography considered here.

Another point that deserves further attention is the validity of the Laplace Tidal Equations in the context of subsurface oceans. The Laplace Tidal Equations are derived from the Navier-Stokes equations assuming: (1) a perfectly homogeneous fluid; (2) horizontal length-scale of the problem larger than vertical length-scale; and (3) small perturbations relative to a state of uniform rotation (e.g., Miles, 1974; Hendershott, 1981; Gerkema et al., 2008). Considering the little amount of information about the composition of subsurface oceans and the premise that they are heated from below it seems reasonable to make the assumption that subsurface oceans are neutrally buoyant (Vance and Goodman, 2009) and thus justify (1). However, depending on the ocean salinity, the ocean might be stably stratified (Melosh et al., 2004; Vance and Brown, 2005). In that case, internal gravity waves might develop. The effect of stratification has been considered by Tyler (2011) who used a scaling law to relate the baroclinic and barotropic ocean response and suggested that baroclinic tides in a stratified ocean could close Enceladus' energy budget. However, it is not clear how the baroclinic response would be excited. The effect of stratification in the ocean response to tides could be further investigated by using a multilayered shallow-water system. Moreover, the flow of the barotropic tide over topography can result in the excitation of internal gravity waves (Egbert and Ray, 2003). The barotropic response of the ocean obtained with our model could be used as starting point to study the excitation of the baroclinic tide through this mechanism.

Assumption (2) leads to the hydrostatic and traditional approximations which filter internal waves from the solution. The LTE have been widely used to study tides on Earth and successfully explain ~70% of tidal dissipation in the ocean, the remaining part being due to internal waves excited in regions of rough topography (Egbert and Ray, 2000,

2003). Taking the radius and ocean thickness as horizontal and vertical length-scales, respectively, we find that the ratio between vertical and horizontal length-scales is ~0.15 for Enceladus as compared to ~0.001 for Earth. Rovira-Navarro et al. (2019) and Rekier et al. (2019) showed that internal inertial waves can be excited in Enceladus but found dissipation due to internal waves to be generally small in the linear regime for oceans of constant thickness. However, non-linear terms neglected under assumption (3) in the Navier-Stokes equations can induce domain filling turbulence (Lemasquerier et al., 2017; Wilson and Kerswell, 2018). The effect of topography on the propagation of inertial waves as well as in triggering turbulence in subsurface oceans remains to be studied.

Declaration of competing interest

The authors declare that they have no known competing financial interests or personal relationships that could have appeared to influence the work reported in this paper.

Acknowledgement

This research has been financially supported by the Space Research User Support program of the Netherlands Organisation for Scientific Research (NWO) under contract number ALW-GO/16-19. We thank the two anonymous reviewers for their comments which helped improving the quality of this manuscript.

Appendix A. Mesh selection and model benchmark

We study the effect of the time step and mesh resolution in the FEM model. To do so we consider the results of Matsuyama (2014) who solved the LTE for an ice-free ocean using a spectral method. We use the solutions obtained with a Rayleigh coefficient of $2.7 \cdot 10^{-7}\ \mathrm{s}^{-1}$. We start by considering the effect of the time step. We select a thick ocean, as it implies a more stringent CFL condition. We consider a 9937 m thick ocean and use a mesh with N=848 elements (Fig. A.7). For this mesh size and ocean thickness, a time step of $0.01T_{En}$ would be needed to fulfill the CFL criteria. We run the model for 300 Enceladan orbits with different time steps and compute the average tidal dissipation using Eq. (12) for each orbital period. The results are shown in Fig. A.8a. For all the different time steps the solution converges to a value of tidal dissipation, however accuracy increases with decreasing time step.

To study the effect of mesh size we select two ocean thicknesses; one close to a resonance peak (h_o=30.35 m) and one far from a resonance peak (h_o=500.18 m) and run the model for 300 Enceladan orbits using different meshes ranging from 246 to 2814 elements (Fig. A.7) and a time step of $0.008T_{En}$. Fig. A.8b and c show the surface average tidal dissipation for the different meshes. We see that for the ocean thickness far from a resonance peak all the meshes converge towards the solution of Matsuyama (2014). In contrast, for the resonant ocean thickness, a higher resolution mesh is needed to converge to the solution.

Based on the previous results we chose to use a time step of $0.008T_{En}$ and a mesh with 848 elements. To assess the numerical error obtained with this model configuration we compute tidal dissipation for subsurface oceans with thickness ranging from 10 m to 10 km and compare the results with those of Matsuyama (2014). We observe a very good agreement between the FEM model and analytic results. For most ocean thicknesses errors are smaller than 3%, however close to resonant peaks errors can be as high as 20%.

(a) $N = 246$ (b) $N = 464$

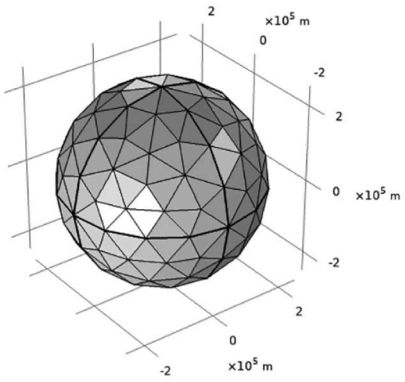

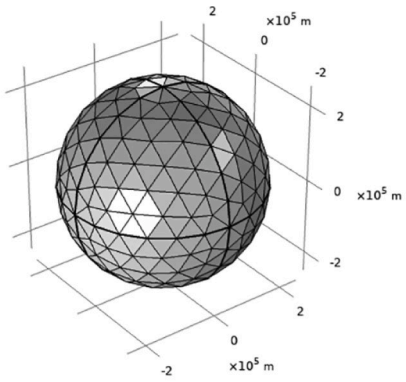

(c) $N = 834$ (d) $N = 2814$

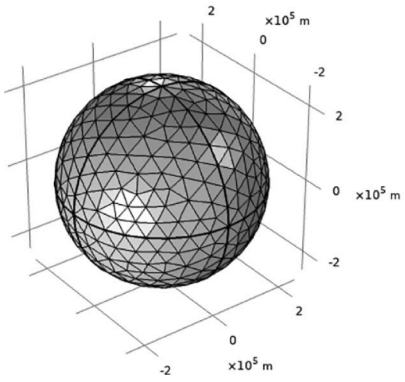

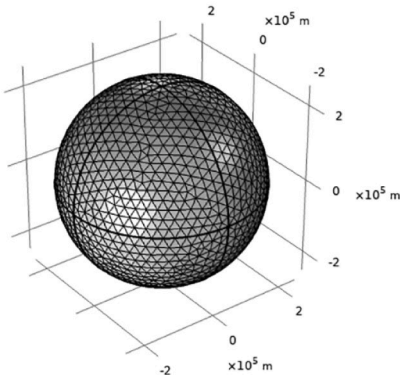

Fig. A.7. Meshes used for the benchmark of the FEM code against analytical results.

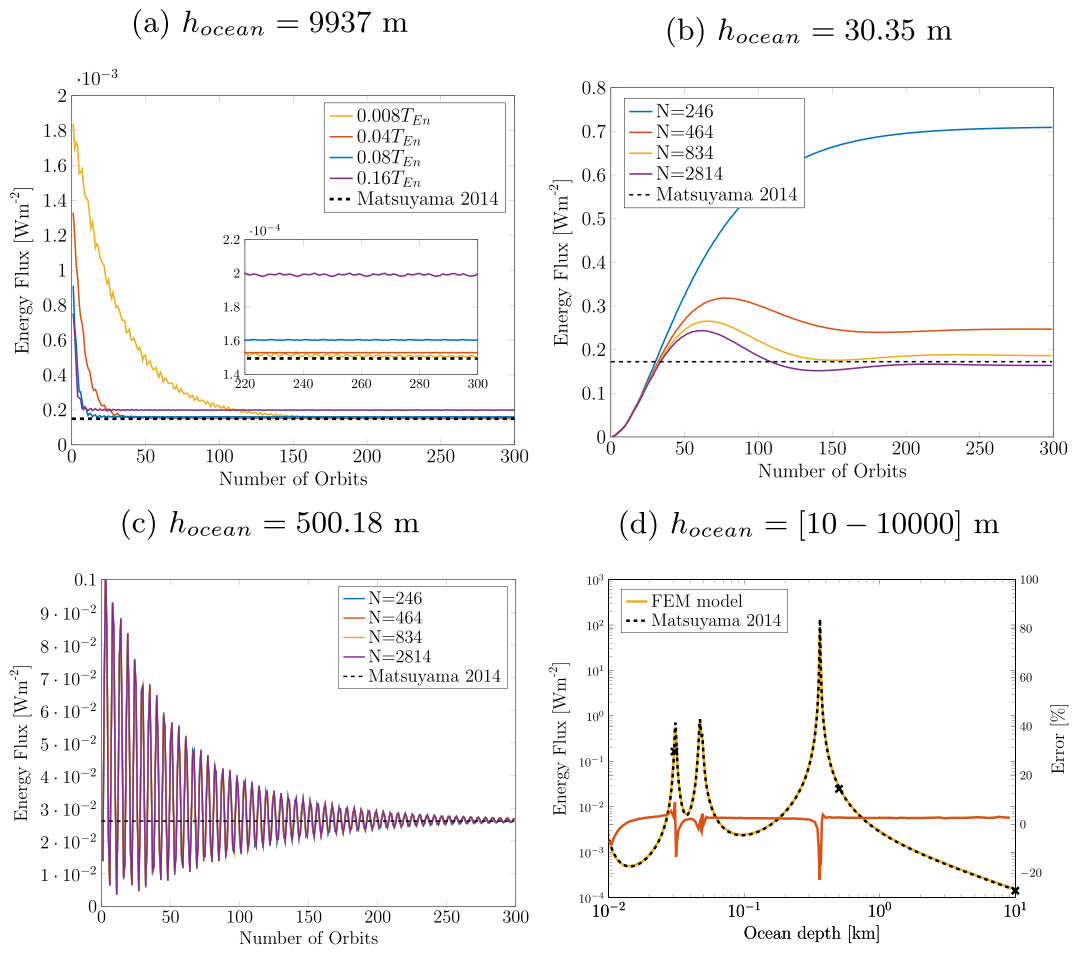

Fig. A.8. (a, b, c) Surface average dissipation obtained using the FEM model for different mesh sizes (represented by number of elements N) and time steps for three different ocean thicknesses. The dashed line corresponds to the analytic solution of Matsuyama (2014). (d) Comparison of the FEM solution obtained with N=848 and a time step of $0.008T_{En}$ and the analytic solutions for ocean thickness between 10 and 10000 m, the error is shown in red and the ocean thicknesses corresponding to the numerical tests of panels a, b and c are indicated with a black crosses.

Appendix B. Resonant modes

(a) $(S2E)_2$ (b) $(S0)_1$

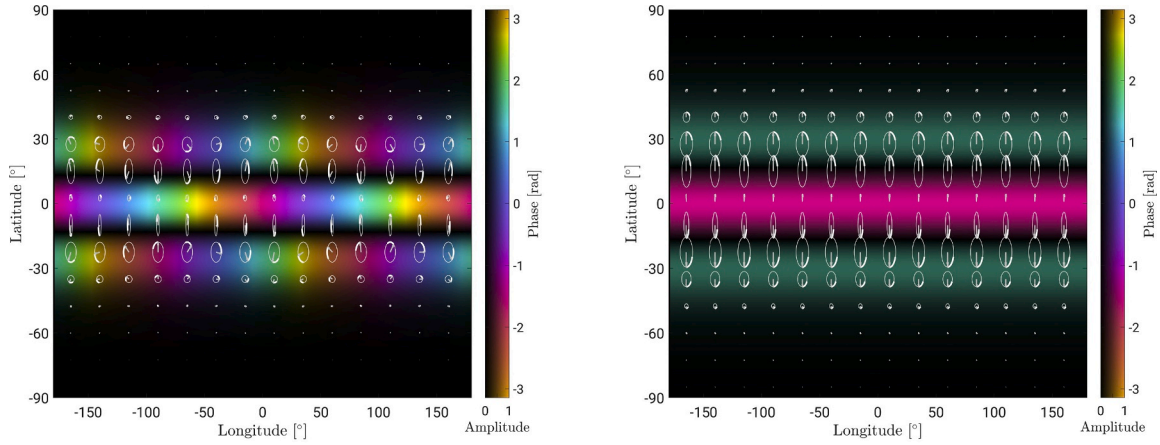

(c) $(S2W)_1$

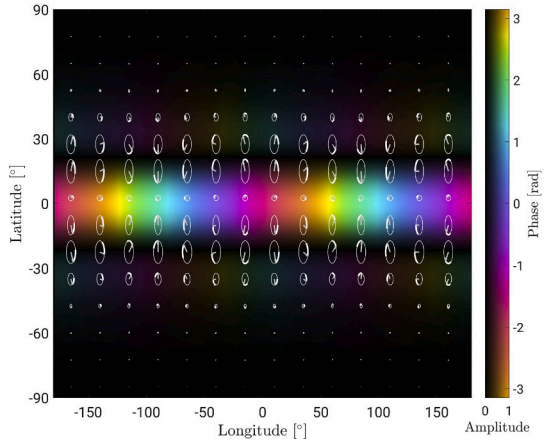

Fig. B.9. Symmetric eigenmodes that can be excited by the eccentricity tide.

(a) $(A1E)_2$ (b) $(A1E)_1$

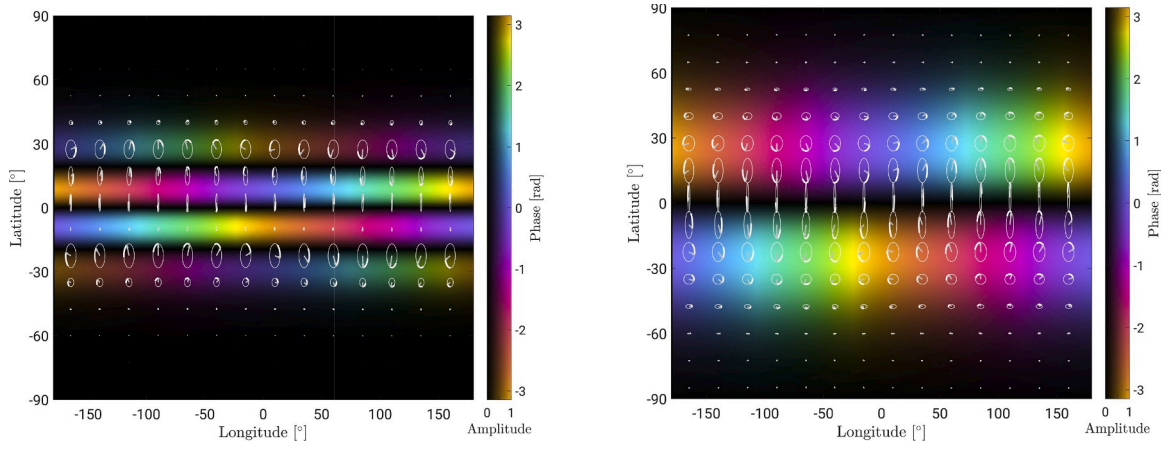

Fig. B.10. Antisymmetric modes excited by the obliquity tide.

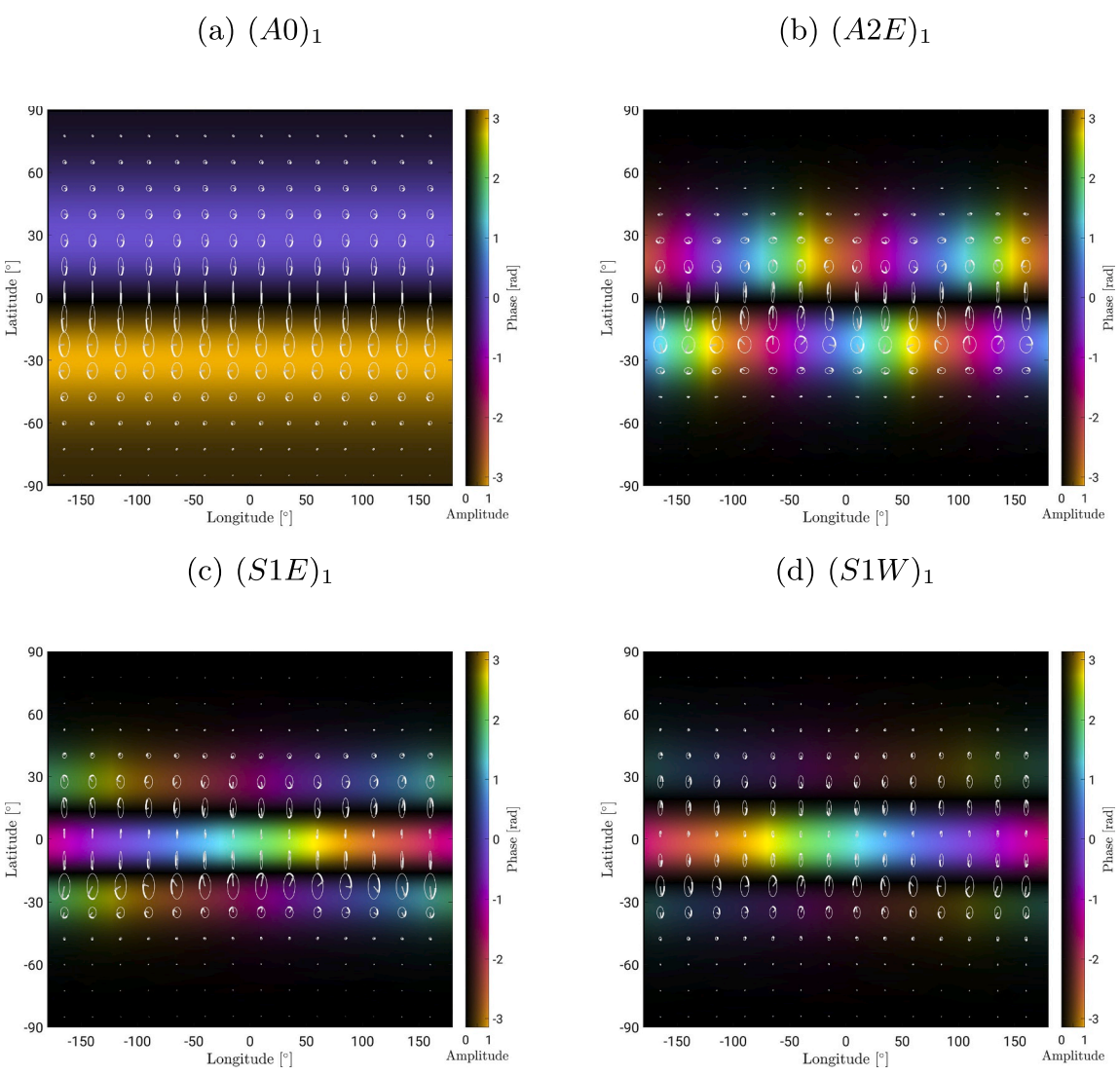

Fig. B.11. Same as Fig. 2 but for four of the extra modes excited by degree three order zero ocean thickness variations.

References

Baland, R.-M., Yseboodt, M., Hoolst, T. V., 2016. The obliquity of enceladus. Icarus 268, 12–31. URL doi:https://doi.org/10.1016/j.icarus.2015.11.039.

Beghin, C., Sotin, C., Hamelin, M., 2010. Titan's native ocean revealed beneath some 45km of ice by a Schumann-like resonance. Cr. Geosci. 342 (6), 425–433. URL doi: https://doi.org/10.1016/j.crte.2010.03.0038.

Běhounková, M., Souček, O., Jaroslav, H., Čadek, O., 2017. Plume activity and tidal deformation on Enceladus influenced by faults and variable ice shell thickness. Astrobiology 17 (9), 941–954. URL doi:https://doi.org/10.1089/ast.2016.1629.

Beuthe, M., 2008. Thin elastic shells with variable thickness for lithospheric flexure of one-plate planets. Geophys. J. Int 172 (2), 817–841. URL doi:https://doi.org/10.1111/j.1365-246X.2007.03671.x.

Beuthe, M., 2016. Crustal control of dissipative ocean tides in Enceladus and other icy moons. Icarus 280, 278–299. URL doi:https://doi.org/10.1016/j.icarus.2016.08.009.

Beuthe, M., Rivoldini, A., Trinh, A., 2016. Enceladus's and Dione's floating ice shells supported by minimum stress isostasy. Geophys. Res. Lett. 43 (19), 10,088–10,096. URL doi:https://doi.org/10.1002/2016GL070650.

Čadek, O., Tobie, G., Van Hoolst, T., Massé, M., Choblet, G., Lefèvre, A., Mitri, G., Baland, R.-M., Běhounková, M., Bourgeois, O., Trinh, A., 2016. Enceladus's internal ocean and ice shell constrained from Cassini gravity, shape, and libration data. Geophys. Res. Lett. 43 (11), 5653–5660. URL doi:https://doi.org/10.1002/2016GL068634.

Cassen, P., Reynolds, R. T., Peale, S. J., 1979. Is there liquid water on Europa? Geophys. Res. Lett. 6 (9), 731–734. URL doi:https://doi.org/10.1029/GL006i009p00731.

Chen, E. M. A., Nimmo, F., 2011. Obliquity tides do not significantly heat Enceladus. Icarus 214 (2), 779–781. URL doi:https://doi.org/10.1016/j.icarus.2011.06.007.

Chen, E., Nimmo, F., Glatzmaier, G., 2014. Tidal heating in icy satellite oceans. Icarus 229, 11–30. URL doi:https://doi.org/10.1016/j.icarus.2013.10.024.

Choblet, G., Tobie, G., Sotin, C., Běhounková, M., Čadek, O., Postberg, F., Souček, O., 2017. Powering prolonged hydrothermal activity inside Enceladus. Nat. Astron. 1 (12), 841–847. URL doi:https://doi.org/10.1038/s41550-017-0289-8.

Chung, J., Hulbert, G. M., 1993. A time integration algorithm for structural dynamics with improved numerical dissipation: the generalized-α method. Journal of Applied Mechanics 60 (2), 371–375. URL doi:https://doi.org/10.1115/1.2900803.

Comsol Multiphysics, 2012. Comsol Multiphysics User's Guide v4.3, 810–815.

Egbert, G. D., Ray, R. D., 2000. Significant dissipation of tidal energy in the deep ocean inferred from satellite altimeter data. Nature 405, 775. URL doi:https://doi.org/10.1038/35015531 http://10.0.4.14/35015531.

Egbert, G. D., Ray, R. D., 2003. Semidiurnal and diurnal tidal dissipation from TOPEX/Poseidon altimetry. Geophys. Res. Lett. 30 (17). URL doi:https://doi.org/10.1029/2003GL017676.

Gerkema, T., Zimmerman, J. T. F., Maas, L. R. M., van Haren, H., 2008. Geophysical and astrophysical fluid dynamics beyond the traditional approximation. Rev. Geophys 46 (2). URL doi:https://doi.org/10.1029/2006RG000220.

Haurwitz, B., 1940. The motion of atmospheric disturbances on the spherical Earth. J. Mar. Res. 3, 254–267.

Hay, H. C., Matsuyama, I., 2017. Numerically modelling tidal dissipation with bottom drag in the oceans of Titan and Enceladus. Icarus 281, 342–356. URL doi:https://doi.org/10.1016/j.icarus.2016.09.022.

Hay, H. C., Matsuyama, I., 2019. Nonlinear tidal dissipation in the subsurface oceans of Enceladus and other icy satellites. Icarus 319, 68–85. URL doi:https://doi.org/10.1016/j.icarus.2018.09.019.

Hemingway, D. J., Mittal, T., 2019. Enceladus's ice shell structure as a window on internal heat production. Icarus 332, 111–131. URL doi:https://doi.org/10.1016/j.icarus.2019.03.011.

Hendershott, M.C., 1981. Long waves and ocean tides. In: Warren, B.A., Wunsch, C. (Eds.), Evolution of Physical Oceanography. MIT Press, Cambridge, Mass, pp. 292–341.

Hough, S. S., 1898. On the application of harmonic analysis to the dynamical theory of the tides. Part II. On the general integration of Laplace's tidal equations. Proc. R. Soc. Lond. 191, 139–185. URL doi:https://doi.org/10.1098/rspl.1897.0099.

Hussmann, H., Spohn, T., Wieczerkowski, K., 2002. Thermal equilibrium states of Europa's ice shell: Implications for internal ocean thickness and surface heat flow. Icarus 156 (1), 143–151. URL doi:https://doi.org/10.1006/icar.2001.6776.

Iess, L., Stevenson, D. J., Parisi, M., Hemingway, D., Jacobson, R. A., Lunine, J. I., Nimmo, F., Armstrong, J. W., Asmar, S. W., Ducci, M., Tortora, P., 2014. The gravity field and interior structure of Enceladus. Science 344 (6179), 78–80. URL doi:https://doi.org/10.1126/science.1250551.

Jara-Orué, H. M., Vermeersen, B. L., 2011. Effects of low-viscous layers and a non-zero obliquity on surface stresses induced by diurnal tides and non-synchronous rotation: The case of Europa. Icarus 215 (1), 417–438. URL doi:https://doi.org/10.1016/j.icarus.2011.05.034.

Khurana, K. K., Kivelson, M. G., Stevenson, D. J., Schubert, G., Russell, C. T., Walker, R. J., Polanskey, C., 1998. Induced magnetic fields as evidence for subsurface oceans in Europa and Callisto. Nature 395 (6704), 777–780. URL doi:https://doi.org/10.1038/27394.

Kivelson, M. G., Khurana, K. K., Russell, C. T., Walker, R. J., Warnecke, J., Coroniti, F. V., Polanskey, C., Southwood, D. J., Schubert, G., 1996. Discovery of Ganymede's magnetic field by the Galileo spacecraft. Nature 384 (6609), 537–541. URL doi:https://doi.org/10.1038/384537a0.

Lainey, V., Ö. Karatekin, Desmars, J., Charnoz, S., Arlot, J.-E., Emelyanov, N., Poncin-Lafitte, C. L., Mathis, S., Remus, F., Tobie, G., Zahn, J.-P., May 2012. Strong tidal dissipation in Saturn and constraints on Enceladus' thermal state from astrometry. The Astrophysical Journal 752 (1), 14. URL doi:https://doi.org/10.1088/0004-637X/752/1/14.

Lainey, V., Jacobson, R. A., Tajeddine, R., Cooper, N. J., Murray, C., Robert, V., Tobie, G., Guillot, T., Mathis, S., Remus, F., Desmars, J., Arlot, J.-E., Cuyper, J.-P. D., Dehant, V., Pascu, D., Thuillot, W., Poncin-Lafitte, C. L., Zahn, J.-P., 2017. New constraints on Saturn's interior from cassini astrometric data. Icarus 281, 286–296. URL doi:https://doi.org/10.1016/j.icarus.2016.07.014.

Laplace, P.-S., 1798. Traité de mécanique céleste, Tome II, Livre IV (Des oscillations de la mer et de l'atmosphére).

Lemasquerier, D., Grannan, A. M., Vidal, J., D. C., Favier, B., Le Bars, M., Aurnou, J. M., 2017. Libration driven flows in ellipsoidal shells. J. Geophys. Res. Planets 122 (9), 1926–1950. URL doi:https://doi.org/10.1002/2017JE005340.

Longuet-Higgins, M. S., 1968. The eigenfunctions of Laplace's tidal equations over a sphere. Philos. Trans. Royal Soc. A 262 (1132), 511–607. URL doi:https://doi.org/10.1098/rsta.1968.0003.

Margules, M., 1893. Luftbewegungen in einer rotierenden Sphäroidschale. Sber. Akad. Wiss. 102.

Matsuyama, I., 2014. Tidal dissipation in the oceans of icy satellites. Icarus 242, 11–18. URL doi:https://doi.org/10.1016/j.icarus.2014.07.005.

Matsuyama, I., Beuthe, M., Hay, H. C., Nimmo, F., Kamata, S., 2018. Ocean tidal heating in icy satellites with solid shells. Icarus 312, 208–230. URL doi:https://doi.org/10.1016/j.icarus.2018.04.013.

Melosh, H., Ekholm, A., Showman, A., Lorenz, R., 2004. The temperature of Europa's subsurface water ocean. Icarus 168 (2), 498–502. URL doi:https://doi.org/10.1016/j.icarus.2003.11.026.

Miles, J. W., 1974. On Laplace's tidal equations. J. Fluid Mech. 66 (2), 241–260. URL doi:https://doi.org/10.1017/S0022112074000176.

Nimmo, F., Spencer, J., 2015. Powering Triton's recent geological activity by obliquity tides: implications for Pluto geology. Icarus 246, 2–10, special Issue: The Pluto System. URL doi:https://doi.org/10.1016/j.icarus.2014.01.044.

Nimmo, F., Thomas, P., Pappalardo, R., Moore, W., 2007. The global shape of Europa: constraints on lateral shell thickness variations. Icarus 191 (1), 183–192. URL doi:https://doi.org/10.1016/j.icarus.2007.04.021.

Nimmo, F., Barr, A.C., Běhounková, M., McKinnon, W.B., 2018. The thermal and orbital evolution of Enceladus: observational constraints and models. In: Enceladus and the Icy Moons of Saturn, Schenk, P. M. and Clark, R. N. and Howett, C. J. A. and Verbiscer, A. J. and Waite, J. H (Ed.), University of Arizona Press, pp. 79–94. https://doi.org/10.2458/azu_uapress_9780816537075-ch005. URL.

Ojakangas, G. W., Stevenson, D. J., 1989. Thermal state of an ice shell on Europa. Icarus 81 (2), 220–241. URL doi:https://doi.org/10.1016/0019-1035(89)90052-3.

Platzman, G. W., 1975. Normal modes of the Atlantic and Indian oceans. J. Phys. Oceanogr. 5 (2), 201–221. URL doi:10.1175/1520-0485(1975)005<0201:NMOTAA>2.0.CO;2.

Platzman, G. W., 1978. Normal modes of the world ocean. Part I. Design of a finite-element barotropic model. J. Phys. Oceanogr. 8 (3), 323–343. URL doi:10.1175/1520-0485(1978)008<0323:NMOTWO>2.0.CO;2.

Rekier, J., Trinh, A., Triana, S. A., Dehant, V., 2019. Internal energy dissipation in enceladus's subsurface ocean from tides and libration and the role of inertial waves. J. Geophys. Res. Planets 124 (8), 2198–2212. URL doi:https://doi.org/10.1029/2019JE005988.

Rossby, C., 1939. Relation between variations in the intensity of the zonal circulation of the atmosphere and the displacement of the semi-permanent centers of action. J. Mar. Res 2, 38–55. URL doi:https://doi.org/10.1357/002224039806649023.

Rovira-Navarro, M., Rieutord, M., Gerkema, T., Maas, L. R., van der Wal, W., Vermeersen, B., 2019. Do tidally-generated inertial waves heat the subsurface oceans of Europa and Enceladus? Icarus 321, 126–140. URL doi:https://doi.org/10.1016/j.icarus.2018.11.010.

Saur, J., Duling, S., Roth, L., Jia, X., Strobel, D. F., Feldman, P. D., Christensen, U. R., Retherford, K. D., McGrath, M. A., Musacchio, F., Wennmacher, A., Neubauer, F. M., Simon, S., Hartkorn, O., 2015. The search for a subsurface ocean in Ganymede with Hubble Space Telescope observations of its auroral ovals. J. Geophys. Res. Space Phys. 120 (3), 1715–1737. URL doi:https://doi.org/10.1002/2014JA020778.

Sears, W. D., 1995. Tidal dissipation in oceans on Titan. Icarus 113 (1), 39–56. URL https://doi.org/10.1006/icar.1995.1004.

Souček, O., Hron, J., Běhounková, M., Čadek, O., 2016. Effect of the tiger stripes on the deformation of Saturn's moon Enceladus. Geophys. Res. Lett. 43 (14), 7417–7423. URL doi:https://doi.org/10.1002/2016GL069415.

Souček, O., Běhounková, M., Čadek, O., Hron, J., Tobie, G., Choblet, G., 2019. Tidal dissipation in Enceladus' uneven, fractured ice shell. Icarus 328, 218–231. URL doi:https://doi.org/10.1016/j.icarus.2019.02.012.

Spencer, J. R., Howett, C. J. A., Verbiscer, A., Hurford, T. A., Segura, M., Spencer, D. C., Sep. 2013. Enceladus heat flow from high spatial resolution thermal emission observations. European Planetary Science Congress 8, EPSC2013–840.

Spohn, T., Schubert, G., 2003. Oceans in the icy Galilean satellites of Jupiter? Icarus 161 (2), 456–467. URL doi:https://doi.org/10.1016/S0019-1035(02)00048-9.

Thomas, P., Tajeddine, R., Tiscareno, M., Burns, J., Joseph, J., Loredo, T., Helfenstein, P., Porco, C., 2016. Enceladus' measured physical libration requires a global subsurface ocean. Icarus 264, 37–47. URL doi:https://doi.org/10.1016/j.icarus.2015.08.037.

Tobie, G., Čadek, O., Sotin, C., 2008. Solid tidal friction above a liquid water reservoir as the origin of the south pole hotspot on enceladus. Icarus 196 (2), 642–652. URL doi:https://doi.org/10.1016/j.icarus.2008.03.008.

Tyler, R. H., Dec. 2008. Strong ocean tidal flow and heating on moons of the outer planets. Nature 456 (7223), 770–772. URL doi:https://doi.org/10.1038/nature07571.

Tyler, R. H., 2009. Ocean tides heat Enceladus. Geophys. Res. Lett. 36 (15), l15205. URL doi:https://doi.org/10.1029/2009GL038300.

Tyler, R., 2011. Tidal dynamical considerations constrain the state of an ocean on Enceladus. Icarus 211 (1), 770–779. URL doi:https://doi.org/10.1016/j.icarus.2010.10.007.

Tyler, R., 2014. Comparative estimates of the heat generated by ocean tides on icy satellites in the outer Solar System. Icarus 243, 358–385. URL doi:https://doi.org/10.1016/j.icarus.2014.08.037.

Vance, S., Brown, J., 2005. Layering and double-diffusion style convection in Europa's ocean. Icarus 177 (2), 506–514. URL doi:https://doi.org/10.1016/j.icarus.2005.06.005.

Vance, S., Goodman, J., 2009. Oceanography of an ice-covered moon. In: Europa, Pappalardo, R. T. and McKinnon, W. B. and Khurana, K. K. (Eds). University of Arizona Press, pp. 459–482. URL http://adsabs.harvard.edu/abs/2009euro.book..459V.

Wilson, A., Kerswell, R. R., 2018. Can libration maintain Enceladus's ocean? Earth Planet. Sci. Lett. 500, 41–46. URL doi:https://doi.org/10.1016/j.epsl.2018.08.012.